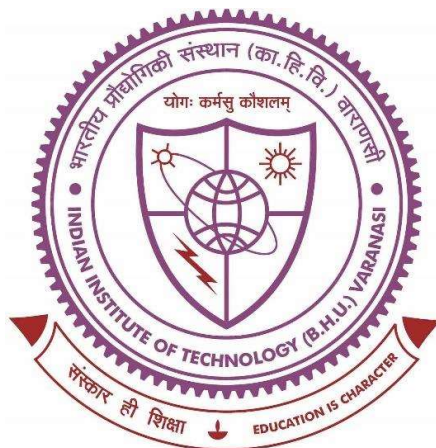


Solution Processing of $\text{Cu}(\text{In}_x\text{Ga}_{1-x})(\text{S},\text{Se})_2$ Absorber Layer for Thin Film Solar Cells



**Thesis submitted in partial fulfillment for the
Award of Degree**

Doctor of Philosophy

Submitted by

Maurya Sandeep Pradeepkumar

**DEPARTMENT OF CERAMIC ENGINEERING
INDIAN INSTITUTE OF TECHNOLOGY
(BANARAS HINDU UNIVERSITY)
VARANASI – 221005
INDIA**

Roll No. 16031005

JULY 2022

CERTIFICATE

It is certified that the work contained in the thesis titled “**Solution Processing of Cu(In_xGa_{1-x})(S,Se)₂ Absorber Layer for Thin Film Solar Cells**” by “**Maurya Sandeep Pradeepkumar**” has been carried out under our joint supervision and that this work has not been submitted elsewhere for a degree.

It is further certified that the student has fulfilled all the requirements of Comprehensive Examination, Candidacy and SOTA for the award of Ph.D. degree.

Supervisor

Dr. Mohammad Imteyaz Ahmad
Assistant Professor
Department of Ceramic Engineering
IIT(BHU), Varanasi

Co-Supervisor

Dr. Joysurya Basu
Associate Professor
Department of Metallurgical Engineering
IIT(BHU), Varanasi

DECLARATION BY THE CANDIDATE

I, **Maurya Sandeep Pradeepkumar**, certify that the work embodied in this Ph.D. thesis is my own bonafide work carried out by me under the joint supervision of **Dr. Mohammad Imteyaz Ahmad** and **Dr. Joysurya Basu** for a period from **July 2016 to July 2022** at the “**Department of Ceramic Engineering**”, Indian Institute of Technology (BHU), Varanasi, India. The matter embodied in this Ph.D. thesis has not been submitted for the award of any other degree/diploma. I declare that I have faithfully acknowledged and given credits to the research workers wherever their works have been cited in my work in this thesis. I further declare that I have not willfully copied any other's work, paragraphs, text, data, results, etc., reported in journals, books, magazines, reports dissertations, thesis, etc., or available at websites and have not included them in this thesis and have not cited as my own work.

Date : July 15, 2022

Place : Varanasi

(MAURYA SANDEEP PRADEEPKUMAR)

CERTIFICATE BY THE SUPERVISORS

This is to certify that the above statement made by the candidate is correct to the best of our knowledge.

(Supervisor)

Dr. Mohammad Imteyaz Ahmad
Assistant Professor
Department of Ceramic Engineering
IIT(BHU), Varanasi

(Co-Supervisor)

Dr. Joysurya Basu
Associate Professor
Department of Metallurgical Engineering
IIT(BHU), Varanasi

Head of Department Ceramic Engineering

COPYRIGHT TRANSFER CERTIFICATE

Title of the Thesis : Solution Processing of $\text{Cu}(\text{In}_x\text{Ga}_{1-x})(\text{S},\text{Se})_2$ Absorber Layer for Thin Film Solar Cells

Candidate's name : Maurya Sandeep Pradeepkumar

COPYRIGHT TRANSFER

The undersigned hereby assigns to the Indian Institute of Technology (Banaras Hindu University), Varanasi all rights under copyright that may exist in and for the above thesis submitted for the award of the *Doctor of Philosophy*.

Date: July 15, 2022

Place: Varanasi

(Maurya Sandeep Pradeepkumar)

Note: However, the author may reproduce or authorize others to reproduce materials extracted verbatim from the thesis or derivative of the thesis for author's personal use provided that the source and the Institute's copyright notice are indicated.

ACKNOWLEDGMENT

First and foremost, I would like to thank my supervisor **Dr. Md. Imteyaz Ahmad**, Assistant Professor, Department of Ceramic Engineering, Indian Institute of Technology (BHU), Varanasi for his continuing moral support and inspiring guidance. I feel fortunate to be the first Ph. D. student of **Dr. Md. Imteyaz Ahmad**.

He has taught me the subject and all aspects of research over last six years. The freedom that he extended to me has helped me immensely to grow as an independent researcher. I do not have enough words to express my deep sense of gratitude to him for shaping my career in such a fruitful manner. He will remain forever my friend philosopher and guide. Second, I thank my co-advisor, **Dr. Joysurya Basu**, Associate Professor, Department of Metallurgical Engineering, Indian Institute of Technology (BHU), Varanasi for his extensive guidance and keen scientific insights through the years. Special thanks to **Dr. J Basu** for his untiring efforts and patience in training me in transmission electron microscopy.

I would like to take this opportunity to put on record my sense of thankfulness and gratitude for **Dr. Santanu Das**, Assistant Professor, Department of Ceramic Engineering, Indian Institute of Technology (BHU), Varanasi for his guidance and support to accomplish this report.

I would also like to thank **Dr. Pradip Kumar Roy** and **Dr. Ashutosh Kumar Dubey** Associate Professor, Department of Ceramic Engineering, Indian Institute of Technology (BHU), Varanasi for their regular evaluation and equally valuable advice. I also take the opportunity to thank **Dr. Manoj Kumar** Associate Professor, Department of Chemical Engineering, Indian Institute of Technology (BHU), Varanasi for their advice during the report evaluation each semester.

I sincerely acknowledge **Dr. Arjun Dey**, Scientist (F) at ISRO Satellite Centre, Bangalore, for motivating me for my Ph.D. during my master thesis. He will remain forever my friend and guide. I would like to convey my sincere regards to **Dr. Anoop Kumar Mukhopadhyay**, Senior Professor, Department of Physics, Sharda University, Greater Noida for extending me his idea on many occasions.

I would like to express my sincere thanks to **Dr. V K Singh**, HoD, and former HoD **Dr. Devendra Kumar** and **Dr. Ram Pyare**, Department of Ceramic Engineering, Indian Institute of Technology (BHU), Varanasi for extending me necessary administrative support.

I am highly grateful and my sincere thanks to **Mr. Lalit Singh** (Dept. of Metallurgical Engineering) and **Mr. Bhagmal** (Dept. of Ceramic Engineering) for their technical help while doing TEM and XRD.

I would like to extend my sincere thanks to **Professor Rajiv Prakash**, Professor in-charge, Central Instrument Facility, Indian Institute of Technology (BHU), Varanasi for his support and permission to use the characterization facility. I thank **Mr. Anirban Roy**, **Mr. Vinay Sharma**, **Mrs. Payal Sharma**, **Mr. Girish Sahu**, **Mr. Nirmal Mallick**, **Mr. Sudhakar** and all technical staff for the continuous support of the characterization facility. Without their help, I am sure the thesis would not have taken the present shape.

I wish to thank my colleagues **Mr. Anurag Kumar**, **Mr. Asim Aftab**, **Mr. Ashwani Gautam**, **Mr. Mukesh Suthar**, **Mr. Deepak Khare**, **Mr. Uttam Sharma**, **Mr. Azaz**, **Mr. Sooraj**, **Mr. Harsh**, **Mr. Harsh Baldi** from Department Ceramic of Engineering, and **Mr. Ankit Singh**, **Mr. Avnish Singh**, **Mr. Amanlal** from Department of Metallurgical Engineering, and **Mr. Adnan Hasan** from ISRO, Bangalore and others for their support and friendship.

I would like to thank my best friend **Anurag, Deepak, Sourabh, Abhiram, Uttam, Avik, Ravi** from bottom of my heart to stand with me for financial and moral support during my thesis work.

Finally, I wish to express my profound thanks to my parents, my younger sister and her family, and other family members for their moral support and continuous encouragement while carrying out this study.

I also would like to thank my beloved wife **Anjali** and her family, for always providing me the moral and unconditional support at each step of my life, and thanks to her for gifting me such a beautiful gift in form of a little and sweet daughter (**Apoorva**), whose smile always teach me there is another part of life present.

I hope I have not overlooked anyone but if I have, it is not for a lack of appreciation. In case of any omission, I sincerely beg my perdon and I truly believe that it is purely incidental on my part.

(MAURYA SANDEEP PRADEEPKUMAR)

TABLE OF CONTENTS

LIST OF FIGURES

LIST OF TABLES

PREFACE

Chapter I	1
I.1 Introduction	1
I.2 Evolution of Solar Cell Technology.....	2
I.3 Principle of Solar Cell Operation	3
I.4 Solar Cell: Absorber Material	9
I.4.1 Wafer-based Solar Cell.....	9
I.4.2 Thin-film Solar Cells.....	11
I.4.3 Copper Indium Gallium Diselenide.....	12
I.5 Motivation	16
I.6 Challenges and Issues.....	17
I.7 Scope and Objectives	18
I.8 Organization of the Thesis.....	19
Chapter II	21
II.1 Brief History.....	21
II.2 Device Structure	23
II.3 Structural Properties of $\text{CuIn}_x\text{Ga}_{1-x}(\text{S}, \text{Se})_2$ Absorber Layer	26

II.3.1 Crystal Structure.....	26
II.3.2 Phase Diagram	28
II.3.3 Defects in $\text{CuIn}_x\text{Ga}_{1-x}(\text{S}, \text{Se})_2$	30
II.3.4 Band Diagram and Interface of CIGS/CdS	32
II.4 Deposition Techniques for CIGS Absorber Film.....	35
II.4.1 Vacuum-based Deposition Techniques.....	35
II.4.2 Non-Vacuum (Solution)-based Deposition Techniques	39
II.5 Ink-based Solution Processing Routes	42
II.6 Concluding Remarks.....	47
Chapter III.....	48
III.1 Materials	48
III.2 Synthesis of wz- $\text{Cu}(\text{In}_x\text{Ga}_{1-x})\text{S}_2$ NPs and Ink Preparation.....	49
III.2.1 Hot Injection Method.....	49
III.2.2 Schlenk Line Set-up.....	49
III.2.3 Synthesis of wz- $\text{Cu}(\text{In}_x\text{Ga}_{1-x})\text{S}_2$ NPs	51
III.2.4 Nanoparticle Ink Formation.....	53
III.3 Spray Coating	53
III.4 Selenization.....	54
III.5 Chemical Bath Deposition.....	56
III.6 Radio Frequency Sputtering	58

III.7 Thermal Evaporation	60
III.8 Characterization Techniques.....	61
III.8.1 X-ray Diffraction and Grazing Incidence-XRD	61
III.8.2 Field Emission Scanning Electron Microscopy.....	63
III.8.3 Transmission Electron Microscopy	66
III.8.4 X-ray Photoelectron Spectroscopy	68
III.8.5 Fourier Transform Infrared Spectroscopy	69
III.8.6 Differential Scanning Calorimetry.....	71
III.8.7 UV/Visible Spectroscopy	72
III.8.8 Raman Spectroscopy.....	73
III.8.9 Solar Cell Characterization	73
Chapter IV.....	75
IV.1 Introduction	75
IV.2 A Review of Relevant Literature.....	77
IV.3 Experimental Procedure	80
IV.4 Results	81
IV.4.1 XRD Analysis.....	81
IV.4.2 FTIR Analysis.....	84
IV.4.3 TEM Analysis.....	91
IV.5 Discussion.....	102

IV.6 Concluding Remarks	106
Chapter V	107
V.1 Introduction.....	107
V.2 A Review of Relevant Literature	108
V.3 Experimental Procedure.....	109
V.4 Results and Discussion	109
V.5 Concluding Remarks.....	127
Chapter VI	129
VI.1 Introduction	128
VI.2 A Review of Relevant Literature.....	130
VI.3 Experimental Procedure	131
VI.4 Characterization.....	134
VI.5 Results and Discussion	134
VI.6 Concluding Remarks	148
Chapter VII	150
VII.1 Introduction	150
VII.2 A Review of Relevant Literature	152
VII.3 Experimental Procedure	154
VII.3.1 Wurtzite-CIS Nanoparticle Ink Preparation.....	154
VII.3.2 Processing of Absorber Layer.....	154

VII.4 Fabrication of wz-CIS and ch-CISSe Device.....	155
VII.5 Results and Discussion.....	155
VII.5.1 Absorber Layer wz-CIS and ch-CISSe	155
VII.5.2 Buffer Layer Deposition by CBD	170
VII.5.3 Window Layer Deposited by RF Sputtering.....	175
VII.5.4 CuIn(S,Se) ₂ Device Characterization	177
VII.6 Concluding Remarks	179
Chapter VIII.....	181
VIII.1 Brief Summary and Conclusions	181
VIII.2 Suggestions for Future Work	184

REFERENCES

LIST OF PUBLICATIONS

LIST OF FIGURES

Figure I.1 (a) Percentage of total electricity produced by the world using renewable and non-renewable sources. (b) Total energy consumption over the world in the year 2020 (Mtoe: megatonne of oil equivalent). Data adapted from Ref. [1] and [2].
2

Figure I.2 (a) p-n junction formation, (b) Space charge distribution of a p-n junction in equilibrium, (c) Electric field and (d) Potential distribution of an abrupt P-N junction, (e) Energy band diagram of a p-n junction in the thermal equilibrium.5

Figure I.3 (a) Equivalent circuit diagram of a photovoltaic cell: a current source in parallel with a diode. (In practice, no solar cell is ideal so a shunt resistance (R_{sh}) and a series resistance (R_s) are also included), (b) J-V characteristics under dark and light conditions.....8

Figure I.4 (a) Schematic of silicon-based PVs device structure, (b) Market share of PVs panels by technology type. Data source: IEA, USA. 11

Figure I.5 (a) Progress in thin-film solar cell efficiencies of a-Si, CdTe and CIGS (Data adapted from Ref. [29] and[30], (b) Absorption coefficient as a function of bandgap (Data adapted from Ref. [31]), (c) Spectral response of thin-film and silicon solar cell over solar irradiance spectrum(Data adapted from Ref.[32]), (d) Schematic architecture of a CIGS solar cell. 14

Figure I.6 Schematic of proposed nanoparticle ink route for synthesizing CIGS absorber layer..... 17

Figure II.1 The unit cell of the polymorphs of $CuInS_2$: (a) Wurtzite (b) Zincblende (c) Chalcopyrite.27

Figure II.2 (a) Pseudobinary phase diagram $Cu_2S-In_2S_3$, the Phase diagram of Cu-In-S system, (b) Gibbs phase triangle of the system Cu-In-S. Adapted from Ref [89].....28

Figure II.3 (a) Pseudobinary phase diagram $\text{Cu}_2\text{Se}-\text{In}_2\text{Se}_3$, Phase diagram of Cu-In-Se system ((b) Gibbs phase triangle of Cu-In-Se system at room temperature. Adapted from Ref [96].	30
Figure II.4 (a) Typical architecture CIGS solar cell, (b) Ga content profile of the CIGS absorber layer used in simulation (The blue and brown arrows show the ranges of C_m (middle of CIGS absorber layer) and X_m (different distances from back contact)) respectively, Adapted from Ref [113]), (c) Energy band-diagram of a CIGS solar cell with p-type absorber/n-type buffer/n-type window structure between two metallic contacts after.	33
Figure II.5 (a) Schematic setup of the co-evaporation process, (b) Three stage process in which In and Ga are deposited in the first and third stage, whereas Cu is deposited in the second stage.	37
Figure II.6 (a) schematic set-up of the sputtering system, Two-step process (sequential selenization), (b) selenization from the vapor of H_2Se , (c) selenium evaporation and a rapid thermal process (RTP) in an inert atmosphere.	38
Figure II.7 Number of available solution deposition techniques used for precursor and nanoparticle ink deposition. Reproduced with permission [144]. Copyright 2011, Royal Society of Chemistry.	40
Figure II.8 Evolution of record efficiency $\text{Cu}(\text{In,Ga})(\text{S,Se})_2$ solar cells from molecular-ink routes comparing with vacuum-based solar cells shown as a reference. Reproduced with permission [137].	44
Figure II.9 Schematic diagram comparing (a) the molecular and (b) nanoparticle solution CIGS deposition approach.	46
Figure III.1 (a) Schematic representation and (b) experimental setup of Schlenk line for the synthesis of $wz\text{-Cu}(\text{In}_x\text{Ga}_{1-x})\text{S}_2$ nanoparticles.	50
Figure III.2 Flowchart of producing $\text{Cu}(\text{In}_x\text{Ga}_{1-x})\text{S}_2$ NPs from metal precursor through the hot-injection method and color change observed during reaction with respect to temperature	52

Figure III.3 (a) Schematic representation and (b) a picture of the spray pyrolysis system utilized for the deposition of wz-Cu(In _x Ga _{1-x})S ₂ film.	53
Figure III.4 (a) Schematic diagram of selenization set-up with flowing argon gas, (b) Experimental set-up with graphite box containing selenium shots and wz-CIS film, (c) Photograph of high temperature tube furnace, (d) Temperature profile for the selenization process..	55
Figure III.5 Flowchart of formation CdS thin film through fast annealing process	56
Figure III.6 (a) Schematic and (b) picture setup of chemical bath deposition, (c) Schematic and (d) Photograph setup of radiative annealing of CdS layer.	57
Figure III.7 (a) Schematic diagram and (b) Instrument photograph of RF magnetron sputtering system	59
Figure III.8 (a) Schematic and (b) Photograph of the thermal evaporation system used for front contact in CIS device.	60
Figure III.9 (a) Bragg-Brentano geometry and (b) photograph of bench-top XRD, (c) Grazing incident geometry and (d) photograph of Grazing Incidence XRD. ..	63
Figure III.10 (a) Schematic of SEM eliciting the incidence of electrons through various electromagnetic lenses, followed by scanning the sample surface and gathering the signals to generate the final image, (b) Interactions of electrons with matter in a scanning electron microscope with various signals, (c) Photograph of Field Emission Scanning Electron Microscope.	65
Figure III.11 (a) Schematic representing path of an electron beam in TEM, (b) Photograph of actual TEM machine with complete cabinet assembly.....	67
Figure III.12 Schematic diagram showing (a) the components of a typical photoelectron spectroscopy set-up, (b) photoemission process used for XPS.	69
Figure III.13 (a) Schematic representation and (b) Instrumental picture of FT-IR spectrometer.....	70

Figure III.14 (a) Schematic of heat-flux, (b) Actual photograph of Differential scanning calorimetry.....	72
Figure III.15 Picture of solar simulator for IV characteristic.....	74
Figure IV.1 X-ray diffraction patterns, demonstrating the progressive evolution of peaks of CuInS ₂ nanoparticles as taken from the reaction mixture at temperatures (a) 160 °C, (b) 200 °C, (c) 250 °C, (d) 290 °C, (e) 310 °C. (The red, blue and black solid line a at the bottom of (a) are the simulated diffraction patterns of the wurtzite phase of Cu ₂ S, In ₂ S ₃ and CIS respectively. Crystal structure of wz-CIS (right top corner) and Cu ₂ S (right bottom corner), where Cu and In atoms occupy the same position, and each occupation is 50% in case wz-CIS).	83
Figure IV.2 FTIR spectra of (a) OAm, (b) TOPO, reaction mixture that consist of Cu(acac)+In(acac)+TOPO + OAm at (c) 50 °C, (d) 100 °C, (e) 150 °C.....	86
Figure IV.3 FT-IR spectra of pure t-DDT as the sulfur source	87
Figure IV.4 Infrared absorption spectra of pure form of (a)1-DDT, (b) t-DDT, and reaction mixture of Cu(acac) and In(acac) in TOOP and OAm with thioils at (c) 160 °C, (d) 200 °C, (e) 250 °C, (f) 290 °C, (g) 310 °C.	89
Figure IV.5 FT-IR spectra of pure 1-DDT as the sulfur source.	90
Figure IV.6 (a) BF-TEM micrographs demonstrating the evolution of size distribution, (b) corresponding SAED pattern, (c) length and (d) width distribution histogram of oval-shaped nanoparticles at 160 °C, and (e) BF-TEM image, (f) SAED pattern, (g) length and and (h) width distribution histogram of oval-shaped nanoparticle at 200 °C.....	92
Figure IV.7 (a) BF-TEM image with inserted SAED pattern, (b) HRTEM image of a CIS NP showing facets and preferential growth along c-direction and (inset) Fast Fourier transform (FFT) pattern. Misfit dislocation are marked with a dotted circle (right bottom of Figure IV.7 (b), red arrows represent the amorphous layers on the surface, (c) length and (d) width distribution histogram of oval-shaped nanoparticle at 250 °C.	94

Figure IV.8 (a)BF-TEM image with SAED pattern (inset), (b) HRTEM image of a CIS NP shows that the facets preferentially grow along c-direction. FFT of the image is shown in the inset. Misfit dislocations are marked with white dotted circles and red arrows represent the amorphous layers on the surface. (c) Length and (d) Width distribution histogram of oval-shaped nanoparticle after synthesis at 290 °C.96

Figure IV.9 (a) BF-TEM image with SAED pattern (inset), (b) HRTEM image of CIS NPs show mildly faceted growth and preferential growth along c-direction. Fast Fourier transform (FFT) of the image is given in the inset. Red arrows indicate the amorphous layers on the surface. (c) length and (d) width distribution histogram of the oval-shaped nanoparticle after processing at 310 °C.....97

Figure IV.10 (a) The detailed evolution of the length and width of the nanoparticles, (b) Variation of Cu/In ratio, and (c) variation of crystallite size as a function of reaction temperature. 101

Figure IV.11 (a) BF-TEM image, (b) HAADF image, (c) EDS spectra, and (d–f) STEM-EDS mapping of Cu–In–S NPs at 310 °C..... 102

Figure IV.12 Schematic representation of formation of wz-CIS NPs through formation of copper sulfide..... 105

Figure V.1 (a) X-ray diffraction of $\text{CuIn}_x\text{Ga}_{1-x}\text{S}_2$ as synthesized wurtzite NPs with varying x, (b) Magnification image of the (0002), (11 $\bar{2}$ 0), and (10 $\bar{1}$ 3) peaks show a clear shift toward a higher angle. 110

Figure V.2 Deconvolution of XRD peaks corresponding to (0002), (1120), and (1013) planes for $\text{CuIn}_{0.7}\text{Ga}_{0.3}\text{S}_2$ (a–c), $\text{CuIn}_{0.5}\text{Ga}_{0.5}\text{S}_2$ (d, e), and $\text{CuIn}_{0.3}\text{Ga}_{0.7}\text{S}_2$ (g–i). 112

Figure V.3 Calculation of composition for In-rich, In-Ga(1:1) and Ga- rich using lattice constant a=b (a) and c (b) by implying Vegard’s law. 113

Figure V.4 Theoretical relative intensities of the XRD peaks of (a) X=0.7, (b) X=0.5, and (c) X=0.3 were calculated using structure factor (F), multiplicity(p),

polarization and Lorentz factor assuming the absorption and temperature factor for both phases being equal for In-rich and In.	115
Figure V.5 Phase fraction of In-rich, In–Ga, and Ga-rich phase as a function of Ga Substitution.	116
Figure V.6 (a) BF-TEM image, (b) SAED pattern of CIS nanocrystals, (c) HRTEM image of a CIS NPs shows a lattice inter-planar spacing of 0.32 nm, (d) fast Fourier transform (FFT) patterns are calculated from the HRTEM image.	117
Figure V.7 (a) BF-TEM image, (b) SAED pattern of CGS nanocrystals, (c) HRTEM image of CGS nanoparticles shows a lattice inter-planar spacing of 0.31 nm, (d) FFT patterns calculated from the HRTEM image.	118
Figure V.8 (a) BF-TEM image inserted SAED pattern of CIGS NPs, (b) HRTEM image of an In-rich nanoparticle shows a lattice inter-planar spacing of 0.33 nm, (c) HRTEM image of an In–Ga nanoparticle shows a lattice inter-planar spacing of 0.29 nm.	120
Figure V.9 (a) BF-TEM image, (b) SAED pattern of CIGS nanocrystals of $\text{CuIn}_{0.5}\text{Ga}_{0.5}\text{S}_2$ NPs, (c) HRTEM image of a hexagonal/equiaxed shows a lattice inter-planar spacing of 0.32 ± 0.01 nm, (d) HRTEM image of a rod-like nanoparticle shows a lattice inter-planar spacing of 0.29 ± 0.01 nm.	121
Figure V.10 (a) BF-TEM image, (b) SAED pattern of CGS nanocrystals of $\text{CuIn}_{0.3}\text{Ga}_{0.7}\text{S}_2$ NPs, (c) HRTEM image of a hexagonal/equiaxed shows a lattice inter-planar spacing of 0.32 ± 0.01 nm, (d) HRTEM image of a rod-like nanoparticle shows a lattice inter-planar spacing of 0.29 ± 0.01 nm.	122
Figure V.11 (a) BF-TEM image, (b) SAED pattern, and (c) HAADF-STEM image of indium-rich composition, (d–g) STEM-EDS mapping of rod-shape nanoparticle.	124
Figure V.12 (a) BF-TEM image, (b) SAED pattern, (c) HAADF-STEM image of gallium-rich composition, (d–g) STEM-EDS mapping of hexagon-shape NP ...	125

Figure V.13 UV–Vis absorption spectra and Tauc plots (in the insert) of wurtzite nanoparticle of CIS (a), CuIn _{0.7} Ga _{0.3} S ₂ (b), CGS (c) of the as-synthesized.	126
Figure VI.1 Schematic of (a) spray system for the deposition of wz-CIS thin film, (b) the selenization process for the preparation of a ch-CISSe absorber film, (c) Top view of graphite box showing the position of selenium and sample.	133
Figure VI.2 (a) X-ray diffraction pattern and (b) FE-SEM image of a cross-section view of the sprayed wz-CIS thin film on soda-lime glass.	135
Figure VI.3 (a) XRD patterns of Ch-CISSe prepared by atmospheric selenization of sprayed wz-CIS layers at a variable temperature of 350, 400, 450, 500, and 550°C for 15 minutes. (b) Magnified view of the (112), (220), and (312) peaks showing a clear shift toward a lower angle.	137
Figure VI.4 Cross-sectional FE-SEM images of (a) as-deposited wz-CIS film, ch-CISSe thin films obtained at varying selenization temperatures (b) 350, (c) 400, (d) 450, (e) 500 and (f) 550 °C. (g) atomic percent of sulfur and selenium in the fine-grained and the large-grained ch-CISSe layers. (Yellow dotted parallel line represents the twinning defect (magnified image X) and ellipse represents the surface restructuring (magnified image Y)).	139
Figure VI.5 (a) FESEM image (b) XRD (c) EXD of selenized ch-CISSe at 400 °C for 45 minutes.	143
Figure VI.6 (a) Vapour pressure of selenium(calculated using equation [275]) and thickness of large grain layer versus selenization temperature. DSC curve (b) of Selenium powder and (c) pure wz-CIS NPs shows the phase transformation from wurtzite to chalcopyrite. The magnified view of the transformation range has been given in the inset. (d) DSC thermogram wz-CIS NPs added with Se powder at varying heating ramp rates of 5, 10, 15, and 20 °C/min with an inset of phase transformation temperature with respect to the varying heating rate. (X=Dehydration of water and Y= Desorption thiols molecules).	144
Figure VI.7 Crystal structures of (a) chalcopyrite CISSe (b) zincblende CISSe and (c) wurtzite CIS.	146

Figure VI.8 (a) XRD pattern of wz-CIS deposited on molybdenum coated SLG and selenized ch-CISSe film at 550 °C for 15 min (b) FESEM image of sprayed wz-CIS with cross-section view at the inset, deposited on molybdenum coated SLG (c) FESEM images of plane and cross-section view of ch-CISSe thin films obtained at 550 °C for 15 min (d) The elemental composition of the wz-CIS and ch-CISSe film.	147
Figure VII.1 SEM images of as-deposited CIS thin films obtained using different spray conditions: variation of 1-DDT solvent (a) 2ml, (d) 4ml, (g) 6ml and (j) 8ml, substrate temperatures 250 °C for (a) and 300°C for (d, g, and j), SEM image of selenized sample(A-D) at 550°C for 15 minutes such as (sample A (b, c), sample B(e, f), sample C(h, i), sample D(k, l).	157
Figure VII.2 SEM images of (a, c) as-deposited wz-CIS and (b, d) selenized ch-CISSe thin films obtained using different spray ink concentrations: sample F and G that has set the inorganic load of inks prepared from wz-CIS NPs to 3.4 mg/ml and 2.8 mg/ml respectively.....	158
Figure VII.3 (a) X-ray pattern of molybdenum coated soda-lime glass at different annealing temperature, (b-c) Top view, (d) Cross-section of delamination of the Mo/CISSe from the glass substrate after selenization, (e) XRD pattern of thick layer of MoSe ₂ layer.	160
Figure VII.4 FE-SEM image of a cross-section view of (a) wz-CIS and (b) ch-CISSe, respectively, (c) X-ray diffraction pattern, (d) Raman spectra of the sprayed wz-CIS and selenized ch-CISSe thin film on soda-lime glass.....	163
Figure VII.5 (a) BFTEM image (b) SAED pattern and (c) HRTEM image of sprayed CIS, (d) BFTEM image (e) SAED pattern and (f) HRTEM image of selenized ch-CISSe.	164
Figure VII.6 XPS spectra of (a) survey spectrum (b) C 1s (c) Cu 2p (d) In 3d of CIS films before(wz-CIS) and after selenization(ch-CISSe), (e) XPS spectra of S 2p of wz-CIS, (f) XPS spectra of Se 3p and 3d of ch-CISSe film.....	166

Figure VII.7 Absorption spectra and Tauc plots (in the insert) of (a) wz-CIS (b) ch-CISSe film.	168
Figure VII.8 SEM micrograph of the CdS thin films deposited on the glass substrate at (a-b) pH 8, (c-d) pH 9, (e-f) pH 10 and (g-h) pH 11 and corresponding EDS spectra.....	171
Figure VII.9 (a) Schematic of CdS film formation during CBD, (b) XRD pattern of the CdS thin films deposited at varying pH.....	173
Figure VII.10 Absorption spectra of the CdS thin films deposited at varying pH.	174
Figure VII.11 X-ray diffraction pattern (a and d), SEM image (inert cross-section image) (b and e) and absorption band (insert bandgap diagram) (c and f) of sputtered ZnO and Al-ZnO layer.....	176
Figure VII.12 PV device response for a (a) wz-CIS and (b) selenized ch-CISSe with 2.12 and 7.35% power conversion efficiency respectively under AM1.5 illumination (100 mW/cm^2).	179

LIST OF TABLES

Table I.1 List of the best PCEs achieved by fabricating solar cells utilizing the CIGS absorber layer processed through MI route.	15
Table IV.1 Simulated (CuInS_2 and Cu_2S) and reference (In_2S_3) the diffraction patterns.....	84
Table IV.2 Infrared vibrational assignments for the intermediate and CuInS_2 NPs at different growth stages.....	90
Table IV.3 Detailed analysis of diffraction pattern of wurtzite CuInS_2 and Cu_2S , and In_2S_3	99
Table V.1 Lattice parameters of CIS, CGS and phase separated compositions...	112
Table V.2 Composition analysis of In-rich, In-Ga, and Ga-rich of wz-CIGS....	114
Table VI.1 Variation of lattice parameter and composition of fine-grain layer and large grain layer for selenization temperature.	148
Table VII.1 List of Raman peak position and vibrational mode for chalcopyrite-CISSe and wurtzite-CIS.....	164
Table VII.2 Electrical parameters of wz-CIS and ch-CISSe were calculated from Hall effect measurement.	169
Table VII.3 Thickness, bandgap and resistivity of the CdS films obtained in present and earlier studies using similar deposition technique.....	175
Table VII.4 Performance of PV devices fabricated using wz-CIS and selenized ch-CISSe absorber layers.	179

PREFACE

Solar photovoltaics (PVs) is one of the renewable energy conversion technologies that is gaining importance globally for its low maintenance and longer operating life. The free and profusely abundant solar energy can be collected by PV devices and may directly be converted into electricity. At present, silicon-based PVs account for over 90% of worldwide module production. However, due to their rigidity, costlier fabrication, and inefficient light absorption, thin film solar cells are being explored. Thin film solar cells have low manufacturing cost, less material usage, high absorption coefficient and are scalable. Thin film solar cells have the potential to convert sunlight into electricity at a lower overall cost. Currently, commercially available most efficient (~19%) thin film solar cells are based on polycrystalline $\text{Cu}(\text{In}_x\text{Ga}_{1-x})(\text{S},\text{Se})_2$ (CIGS) absorber layers. CIGS has a direct and tunable bandgap (1.5–2.0 eV), a high absorption coefficient ($\sim 10^5 \text{ cm}^{-1}$), coupled with greater radiation resistance as compared to crystalline silicon solar cells. For fabricating state-of-the-art high efficiency devices, the CIGS layer is deposited by co-evaporation using an elemental source under high vacuum conditions. Vacuum-based processing technologies have high operating costs and are not easily scalable. Solution-based processing techniques have constantly received attention due to low cost, scalability, control on composition and growth. However, the performance of solution-processed CIGS (18.7%, lab scale) absorber-based devices is much lower than the vacuum processed ones (23.35%, lab scale). Several factors that hamper the device performance of solution processed films include elemental impurities, unburnt impurities from solvents and precursors (C, N, O, Cl etc.), the presence of voids and surface roughness, fine-grained layer with high boundary density. We

have tried to mitigate some of the stated issues and demonstrated the processing of solar cell grade high density, large grained absorber layer through spray deposition.

Typically, chalcopyrite(ch), zinc-blende and wurtzite (wz) are the three polymorphs of CIS, with chalcopyrite being the thermodynamically stable form at room temperature (RT). Recently, it has been demonstrated for $\text{Cu}_2\text{ZnSn}(\text{S},\text{Se})_4$ (CZTS) that phase transformation can assist a rapid grain growth. It was shown that wz-CZTS nanoparticles, when heated to about 500 °C in the presence of Se vapour, transform to kesterite phase accompanied by rapid grain growth where grains were shown to grow upto a micrometer in size. Similar to CZTS, the wurtzite phase in CIGS is also a high-temperature phase (stable between 1045-1090 °C) and is metastable at room temperature. The wurtzite phase of CIGS has been reported to stabilize in the nano-regime. Many researchers have recently reported the synthesis of wz-CIGS nanoparticles through wet chemical route.

The first step was to synthesize a phase pure wz-CIS nanoparticle. The metastable wz-CuInS₂ (CIS) nanoparticles were synthesized by a solution-based processing technique. The mechanism of wz-CIS NPs formation during solution processing was studied. The formation of CIS was found to depend on various factors such as temperature, relative reactivity of copper and indium in solution, type of ligand, etc. It was observed from XRD and TEM, Cu₂S nucleated and grew at the earlier stages and later In₂S₃ formed. On increasing temperature above 200 °C, CIS formed with the diffusion of In³⁺ ion. Wurtzite CIS nanoparticles preferentially grew along one direction while the width nearly remained constant. The HRTEM images and the FFT patterns indicated that the oval shaped wz-CIS NPs grew along the [0002] direction and it was enclosed by (10 $\bar{1}$ 1) and (10 $\bar{1}$ 0) crystallographic facets. FTIR

spectra recorded at different stages of synthesis (50–310 °C) pointed towards the ligand exchange mechanism after the addition of sulfur source at 160 °C. The synthesis of wurtzite CIS NPs through the wet-chemical route using amine-thiol ligand confirmed that the CIS NPs formed by incorporation of indium into the Cu₂S crystal nuclei through the diffusion and/or cation exchange.

Once the CIS was synthesized, Ga was substituted for In, and its influence on the structure and morphology of particles was studied. Nanocrystalline CuIn_xGa_{1-x}S₂ (x = 1, 0.7, 0.5, 0.3, 0) wurtzite particles were synthesized by solution process. It was observed that gallium incorporation in CuInS₂ results in structural distortion, non-homogeneous shape, and size distribution of particles. As-synthesized CuInS₂ (CIS) and CuGaS₂ (CGS) nanoparticles were single-phase wurtzite structures, whereas CuIn_{0.7}Ga_{0.3}S₂, CuIn_{0.5}Ga_{0.5}S₂, and CuIn_{0.3}Ga_{0.7}S₂ had three wurtzite phases having In-rich, In–Ga, and Ga-rich compositions. The shape of the resulting nanoparticles were either elongated, polygonal, or tadpole, depending on the phase composition. In-rich particles had elongated rod-like morphology, the In–Ga particles were irregular hexagonal, while the Ga-rich phase formed with a tadpole morphology. It has been observed that the morphological evolution strongly depends on the nature of the composition separation of In and Ga.

The wz-CIS nanoparticles were dispersed and was uniformly deposited over the Mo/SLG substrate by spray deposition using nitrogen as carrier gas. The wz-CIS film (grain size ≈25nm) was selenized to obtain large-grain chalcopyrite CISSe film (grain size ≈700nm). Wurtzite (CIS) to chalcopyrite (CISSe) phase transformation and grain growth at various selenization temperatures of 350, 400, 450, 500 and 550 °C was studied. XRD and high-resolution scanning electron microscopy

(FESEM) indicated that the grain growth depended on the Se diffusion. By 400 °C, the complete film transformed from wurtzite to chalcopyrite phase; however, the grain growth required greater selenium and temperature. Differential scanning calorimetry (DSC) revealed that the phase transformation temperature was sensitive to the heating rate and had a strong second-order character.

Further, the device was fabricated using the as-deposited wurtzite CIS and selenized chalcopyrite CISSe as absorber films with common device architecture SLG/Mo/(wz-CIS or ch-CISSe)/CdS/i-ZnO/Al-ZnO/Au. The homogenous and compact layer of CdS (~100nm) was deposited in a chemical bath maintained at pH10, which was subsequently dried at 120 °C by radiative annealing. The compact and transparent conductive oxide film, i-ZnO (~60nm) and Al-ZnO (~300nm) were deposited by the RF sputtering, which had a bandgap of 3.3 and 3.45 eV, respectively. Finally, Au front contact was deposited using thermal evaporation. The fabricated device with as-deposited wz-CIS and selenized ch-CISSe absorber layers had PCEs 2.12 and 7.35%, respectively.

The thesis shows the alternative approach for CIS device fabrication, where spray deposition technique utilizing wz-CIS nanoparticle ink is a promising, low-cost and scalable process for the deposition of CIS absorber layers. The layer shows phase transformation and grain growth (micron size) on selenization. The process can be further improved by incorporating multiple ink compositions to regulate Ga/Ga+In gradient to improve the efficiency. Further developments should germinate industrial interest in non-vacuum deposition processes for low-cost solar cell production.